Rayleigh wave phase velocity and error maps up to the fifth overtone.

Stéphanie Durand[1], Eric Debayle[1] and Yanick Ricard[1]

Corresponding author: S. Durand, Laboratoire de Géologie de Lyon - Terre, Planète, Environnement, Université de Lyon, Bâtiment Géode, 69100 Villeurbanne, France. (stephanie.durand@ens-lyon.fr)

[1]Laboratoire de Géologie de Lyon - Terre,
Planète, Environnement, CNRS UMR 5276,
École Normale Supérieure de Lyon,
Université de Lyon, Université Claude
Bernard Lyon 1, 46 Allée d'Italie, 69364
Lyon Cedex 07, France

We present a global dataset of phase velocity maps for Rayleigh waves, with their errors. These maps are obtained from the tomographic inversion of phase velocity curves measured in the period range 40-250 s by *Debayle and Ricard* [2012], completed with new measurements at longer periods, between 150 and 360 s. The full dataset includes $\sim$ 22,000,000 phase velocity measurements combined to build 60 phase velocity maps covering the period range 40-360 s for the fundamental mode and up to the fifth overtone. Each phase velocity map is provided with its *a posteriori* error, resulting in a unique dataset which can be combined with other seismic measurements (surface waves, normal modes, body waves) in regional and global tomographic studies. A preliminary inversion of this dataset shows that it provides constraints on the shear velocity structure down to 1,000 km depth.

1. Introduction

Global seismic models suffer from a decrease of resolution in the transition zone located between ~400 and ~1,000 km depth. Except in very specific regions, like subduction zones [e.g. *Ritsema et al.*, 2004; *Debayle et al.*, 2005], these depths are neither well sampled by the dominant fundamental mode of surface waves nor by teleseismic body waves. It is however possible to achieve a global coverage of the transition zone by extracting more information from surface waves.

A first possibility is to extend the analysis to longer periods. Most datasets derived from surface waves are fundamental mode dispersion curves measured at periods shorter than 200 s [*Trampert and Woodhouse*, 1995; *Ekström et al*, 1997; *Ritzwoller and Levshin*, 1998; *Ekström*, 2011; *Visser et al*, 2008; *Burgos et al*, 2014] which limits the penetration depth to ~250-300 km. It is however possible to increase the sensitivity to the transition zone by measuring the fundamental mode at larger periods up to 360 s [*Nettles and Dziewonski*, 2008].

A second possibility is to extract higher mode information [e.g. *Nolet*, 1975; *Cara*, 1979]. Higher modes are difficult to use because they interfere in the time domain over a broad frequency range. A variety of methods for extracting higher mode dispersion curves has been developed [*Nolet*, 1975; *Cara*, 1979; *Cara and Lévêque*, 1987; *Stutzmann and Montagner*, 1993; *Beucler et al*, 2003; *van Heijst and Woodhouse*, 1997; *Ekström et al*, 1997; *Debayle*, 1999; *Yoshizawa and Kennett*, 2002; *Lebedev et al*, 2005; *Visser et al.*, 2007]. Those using a single seismogram [*van Heijst and Woodhouse*, 1997; *Ekström et al*, 1997; *Debayle*, 1999; *Yoshizawa and Kennett*, 2002; *Lebedev et al*, 2005] achieve the

best coverage and have been used to built the most recent tomographic models [*Ritsema et al.*, 2011; *Debayle and Ricard*, 2012; *Schaeffer and Lebedev*, 2013].

In this manuscript, Rayleigh wave seismograms are analyzed with the automated waveform inversion technique of *Debayle* [1999], modified by *Debayle and Ricard* [2012]. This waveform inversion is based on *Cara and Lévêque* [1987] and provides for a Rayleigh wave seismogram, an average 1-D velocity profile, a set of phase velocity dispersion curves and their associated *a posteriori* errors. We obtain a data base of Rayleigh wave dispersion curves for the fundamental and the five first overtones. For each mode and for each period, we have combined the measured phase velocities in a tomographic inversion to obtain phase velocity maps with their *a posteriori* errors. *A posteriori* errors provide an objective way to weight our maps when combined with other seismic datasets in future global or regional tomographic studies. A preliminary inversion of our Rayleigh wave maps alone shows that they allow to constrain mantle shear velocities down to 1,000 km depth.

2. Datasets

We use a set of dispersion curves measured by *Debayle and Ricard* [2012] from 372,629 Rayleigh waveforms. Phase velocities were measured in the period range 40-250 s for the fundamental mode and up to the fifth overtone. In addition, we apply the same algorithm to 161,730 Rayleigh waveforms recorded for large events ($6.0 < M_w < 7.2$) which excite surface waves at periods greater than 200 s. These waveforms are modeled in the period ranges 120-360 s, 120-240 s and 120-180 s for the fundamental, first and second higher mode, respectively.

The whole dataset includes $\sim$ 22,000,000 phase velocity measurements done on a total of 534,359 Rayleigh wave seismograms. A summary of the number of measurements done for each mode branch is given in Table 1. It is larger than previous Rayleigh wave datasets measured by *van Heijst and Woodhouse* [1999] or *Visser et al* [2008]. It provides new fundamental and higher mode measurements in the period range 120-360 s, which expands the fundamental mode study by *Nettles and Dziewonski* [2008]. It is comparable in size to the datasets of *Schaeffer and Lebedev* [2013] or *Ritsema et al.* [2011], but the modal and frequency contents differ. While *Schaeffer and Lebedev* [2013] analyze up to 14 higher modes in the period range 10-400 s, we limit the number of modes to 6 and the period range to 40-360 s (Figure 1) which should minimize possible biases due to off great circle propagation and mode coupling effects. In addition, this dataset completes that of *Ritsema et al.* [2011] with measurements at longer periods, up to 360 s, and up to the fifth overtone.

Figure 1 displays the mean phase velocities and the periods and modes for which measurements have been made. The mean phase velocities are in general slightly larger than PREM [*Dziewonski and Anderson*, 1981] (purple dashed curves). Part of this difference may be due to the fact that a large portion of our dataset samples the thick and fast cratons of the northern hemisphere continents. The exact values used to plot Figure 1 are provided in supplementary Tables 1 and 2.

For each individual waveform, we extract the phase velocities for the fondamental mode and up to 5 overtones and for a total of 60 periods using the iterative and non-linear inversion scheme of *Tarantola and Valette* [1982]. Our approach to fit the waveform

introduces a number of secondary observables [*Cara and Lévêque*, 1987]. This inversion is only weakly non-linear and we can approximate the *a posteriori* covariance matrix of our inversion at the last iteration. This processing step therefore extracts from each waveform up to 60 phase velocities with their uncertainties (the root square of the diagonal covariance matrix).

To decrease the number of data and improve its robustness, we cluster the seismic paths with close epicenters recorded at a given station [*Debayle and Ricard*, 2012]. We use a cluster radius of 400 km (i.e. close to the horizontal smoothing defined in section 3) and consider that the waves of a given cluster follow the same path and feel the same average dispersion between the epicenters and the station. Within each cluster, we select the best resolved phase velocity at each period and each mode, associated with the smallest *a posteriori* error and only when this *a posteriori* error is smaller than 80% of the *a priori* error. This path clustering allows us to restrict the whole dataset to independent paths, to discard outliers and decreases significantly the number of data and their associated uncertainties (see Table 1).

3. Building Phase Velocity and Error Maps

We combine the selected data (i.e., the phase velocities along seismics paths, measured for each mode and each period) using a continuous regionalization scheme [*Tarantola and Valette*, 1982; *Montagner*, 1986; *Debayle and Sambridge*, 2004]. We obtain smooth phase velocity maps by imposing correlations between neighboring points using a Gaussian *a priori* covariance function controlled by an horizontal correlation length, fixed to 400 km. Increasing the horizontal correlation length leads to smoother tomographic images with

lower amplitude anomalies, but the overall pattern of anomalies remains unchanged. An *a priori* model standard deviation controls the amplitude of the inverted model and is set to 0.05 km s^{-1} , according to the expected variation range of the shear velocity in the upper mantle [*Nishimura and Forsyth*, 1989; *Debayle and Ricard*, 2012].

Figure 2 presents some examples of phase velocity (middle column) and error (right column) maps. First, the phase velocity pattern is in agreement with what is expected from the sensitivity kernels (left column). For instance, for the fundamental mode at 40 s (first row) which has a maximum of sensitivity around 70 km depth, the phase velocity map principally displays the surface tectonics. If we consider a longer period, 280 s (second row), the maximum of sensitivity is now in the transition zone and the the presence of slabs become conspicuous. It can also be noted the similarity between the phase velocity maps of the fundamental mode at 40 s (first row), the third overtone at 90 s (fourth row) and the fifth overtone at 40 s (fifth row) which is related to a similar depth of maximum sensitivity. This conforts us in the quality of the measurements. Concerning the error maps (right column) they are obtained from the diagonal of the *a posteriori* covariance matrix. They are normalized to the *a priori* model standard deviation of 0.05 km s^{-1}. The shading is such that the best resolved regions are in black and the poorly resolved regions in white.

The whole dataset (shear velocity kernels, phase velocity maps, error maps and ray density maps) is presented in supplementary Figure 1. The error maps correlate with the ray density, the phase velocity are better constrained where the ray coverage is denser. Shear velocity sensitivity kernels show that our new dataset modeled for large events at

long periods (fundamental mode up to 360 s) provides additional information on the shear velocity structure in the depth range 100-1,000 km.

4. Depth inversion

The regionalization step leads to 60 maps of phase velocity and error (supplementary Figure 1) for the periods and modes given in Figure 1. We extract at each geographical point, the ensemble of phase velocities measurements and their corresponding errors that are inverted to obtain 1D depth-dependent V_s profile. The juxtaposition of the V_s profiles at each geographical point leads to a 3D model of shear velocities. The local phase velocity perturbation for mode m and period T, $\delta c_T^m(\theta, \phi)$, is related to the radial shear velocity structure by :

$$\delta c_T^m(\theta, \phi) = \int_0^a \delta V_s(\theta, \phi, r) K_T^m(r) dr, \quad (1)$$

where $\delta V_s(\theta, \phi, r)$ is the local shear velocity perturbation at depth r and $K_T^m(r) = \partial c_T^m / \partial V_s(r)$ the corresponding shear wave sensitivity kernel computed in PREM (see e.g., Figure 2, left column). This equation implicitly assumes that the compressional velocity V_p and the density ρ are not inverted for, which is reasonable as the Rayleigh waves are mostly affected by V_s. We also performed an inversion using scaling laws between V_s and V_p and between V_s and ρ and found a shear velocity model almost identical to the one obtained without scaling (see supplementary Figure 3). Thus we choose to fix V_p and ρ to the values of PREM. Before inversion, we perform crustal corrections using phase velocities predicted by the crustal part of the 3SMAC model [*Nataf and Ricard*, 1996]. The corrected phase velocity maps and the associated errors are given in supplementary Figure 2. The uncorrected dataset is shown in supplementary Figure 1.

In order to get an idea of the maximal vertical resolution that we can obtain with our dataset we compute the averaging kernels following *Backus and Gilbert* [1968]. These averaging kernels, $A(r, r_0)$, relate the model which can be estimated from the inversion, $< m >_{r_0}$, to the "true" model, $m(r)$:

$$< m >_{r_0} = \int_0^a A(r, r_0) m(r) \mathrm{d}r, \tag{2}$$

Ideally, we would like $A(r, r_0) = \delta(r - r_0)$ meaning that the data can resolve at each depth an infinitely small length-scale. It is however impossible to reach such a resolution with a finite number of data. The resolution kernels $A(r, r_0)$ result from linear combinations of the sensitivity kernels $K_T^m(r)$. They are computed by minimizing $[A(r, r_0) - \delta(r - r_0)]^2$ [see *Backus and Gilbert*, 1968]. They are displayed in Figure 3. The shortest resolved length-scale increases with depth, ranging from ~50 km at 100 km depth to ~250 km at 1500 km depth. Our dataset is barely insensitive to the structure below 1500 km depth.

To perform the tomographic inversion we must define the covariances matrices. The *a priori* data covariance matrix is diagonal and contains the variance calculated from the error maps shown in supplementary Figure 2. The *a priori* model covariance matrix, C_p, is non-diagonal: a Gaussian correlation function couples the velocity variations at radii r and r' :

$$C_p(r, r') = \sigma^2 \exp\left(-\frac{(r - r')^2}{2L(r_M)^2}\right) \tag{3}$$

where r_M is $(r + r')/2$, L the correlation length that controls the vertical smoothness of the model and σ the *a priori* model standard deviation that controls the amplitude of velocity variations. Based on the results of the averaging kernels we allow the correlation

length L and the *a priori* model standard deviation σ to vary with depth and their values are given in supplementary Table 3.

The shear velocity model obtained from the inversion of our phase velocity maps is displayed in Figure 4. In the upper mantle, the structures are in general agreement with other recent models derived from fundamental and higher Rayleigh modes [*Debayle and Ricard*, 2012; *Schaeffer and Lebedev*, 2013]. For example, we recover the very strong correlation with surface tectonics in the top 200 km, and the high velocity signature of ponding slabs within the transition zone. However, the addition of longer period surface waves up to 360 s provides additional sensitivity down to at least 1,000 km depths. Although these long period surface waves only constrain the broad scale structure at the top of the lower mantle, they are very complementary to other existing seismic datasets. They constrain both even and odd degrees of the shear wave mantle structure while normal mode splitting data are only sensible to the even structure. We plan to combine this surface wave dataset with normal modes and long period S-wave measurements. This will help to better constrain the mantle broad-scale structure, especially at the top of the lower mantle, where the body wave coverage remains uneven.

5. Concluding remarks

We present a set of fundamental and higher Rayleigh mode phase velocity maps derived from the regionalization of $\sim 22,000,000$ phase velocity measurements. This unique dataset has been obtained from the waveform modeling of $\sim 540,000$ waveforms (for a total of 60 periods and 6 modes), following the scheme developped by *Debayle and Ricard* [2012]. We provide an *a posteriori* error map associated with each phase velocity

map. These error maps can be used to weight our phase velocity maps in tomographic inversions combining this dataset with other seismic data in future global and regional studies. Finally, we show that an inversion of our surface wave dataset alone constrains the shear velocity structure down to at least 1,000 km depth. Both the raw measurements and the phase velocity and error maps, with and without crust corrections, are available to the community on request. This dataset could be included for the global modeling of the mantle structure, for example in the recently launched Reference Earth Model initiative.

Acknowledgments. This work was supported by the French ANR SEISGLOB ANR-11-BLANC-SIMI5-6-016-01. Our raw measurements and phase velocity maps are freely available on request to stephanie.durand@ens-lyon.fr. We thank Jeroen Ritsema, an anonymous reviewer and the Associate Editor, Michael Wysession for their constructive reviews.

References

Backus, G. and F. Gilbert, (1968), The resolving power of gross Earth data, *Geophys. J. R. astr. Soc.*, **16**, 169–205.

Beucler, E., E., Stutzmann, J-P., Montagner, (2003), Surface wave higher-mode phase velocity measurements using a roller-coaster-type algorithm, *Geophys. J. Int.*, *155*(1), 289–307.

Burgos, G., J-P., Montagner, E., Beucler, Y., Capdeville, A., Mocquet, M., Drilleau, (2014), Oceanic lithosphere-asthenosphere boundary from surface wave dispersion data, *J. Geophys. Res.*, *119*(2), 1079–1093.

Cara, M., (1979), Lateral variations of S-velocity in the upper mantle from higher Rayleigh modes, *Geophys. J. R. Astron. Soc.*, *57*(3), 649–670.

Cara, M., J.J. Lévêque, (1987), Waveform inversion using secondary observables, *Geophys. Res. Lett.*, *14*, 1046–1049.

Debayle, E., (1999), SV-wave azimuthal anisotropy in the australian upper mantle: Preliminary results rom automated Rayleigh waveform inversion, *Geophys. J. Int.*, *137*(3), 747–753.

Debayle, E., M., Sambridge, (2004), Inversion of massive surface wave data sets: Model construction and resolution assessment, *J. Geophys. Res.*, *109*, B02316, doi:10.1029/2003JB002652.

Debayle, E., B., Kennett, K., Priestley, (2004), Global azimuthal seismic anisotropy and the unique plate-motion deformation of Australia, *Nature*, *433*(7025), 509–512.

Debayle, E., and Y. Ricard, (2012), A global shear velocity model of the upper mantle from fundamental and higher Rayleigh mode measurements, *J. Geophys. Res.*, *117*(B10308), 1–24.

Dziewonski, A. M., and D.I. Anderson, (1981), Preliminary reference Earth model, *Phys. Earth Planet. Int.*, *25*, 297–236.

Ekström, G., J., Tromp, E.W.F., Larson, (1997), Measurements and global models of surface wave propagation, *J. Geophys. Res.*, *102*(B4), 8137–8157.

Ekström, G., (2011), A global model of Love and Rayleigh surface wave dispersion and anisotropy, 25-250 s, *Geophys. J. Int.*, *187*(3), 1668–1686

Kanamori, H, Anderson, D. L., (1977), Importance of physical dispersion in surface-wave and free-oscillation problems, *Rev. Geophys.*, *15*, 105–112.

Lebedev, S., G. Nolet, T., Meier, (2005), Automated multimode inversion of surface wave and S waveforms, *Geophys. J. Int.*, *162*, 951–964.

Maupin, M., (2011), Upper-mantle structure in southern Norway from beamforming of Rayleigh wave data presenting multipathing, *Geophys. J. Int.*, *185*, 985–1002.

Montagner, J., (1986), Regional three-dimensional structures using longperiod surface waves, *Ann. Geophys.*, *4*, 283-294.

Nataf, H-C., and Y., Ricard, (1996), 3SMAC: an a priori tomographic model of the upper mantle based on geophysical modeling, *Phys. Earth Planet. Int.*, *95*, 101-122.

Nishimura, C.E., and D.W., Forsyth, (1989), The anisotropic structure of the upper mantle in the Pacifique, *Geophys. J. Int.*, *96*(2), 203-229

Nettles, M., and A.M., Dziewonski, (2008), Radially anisotropic shear velocity structure of the upper mantle globally and beneath North America, *J. Geophys. Res.*, *113*(B2), 1–27.

Nolet, G., (1975), Higher Rayleigh modes in western-Europe, *Geophys. Res. Lett.*, *2*(2), 60–62.

Ritsema, J., H.J., van Heijst, J.H., Woodhouse, (2004), Global transition zone tomography, *J. Geophys. Res.*, *109*(B02302), 1–14.

Ritsema, J., A., Deuss, H.J., van Heijst, J.H., Woodhouse, (2011), S40RTS: a degree-40 shear velocity model for the mantle from new Rayleigh wave dispersion, teleseismic traveltime and normal-mode splitting function measurements, *Geophys. J. Int.*, *184*,

1223–1236.

Ritzwoller, M., H., and A. L. Levshin, (1998), Eurasian surface wave tomography: Group velocities, *J. Geophys. Res.*, *103*(B3), 4839–4878.

Shaeffer, A.J., and S., Lebedev, (2013), Global shear speed structure of the upper mantle and transition zone, *Geophys. J. Int.*, *194*(1), 417–449.

Stutzmann,E., and J-P., Montagner, (1993), An inverse technique for retrieving higher mode phase-velocity and mantle structure, *Geophys. J. Int.*, *113*(3), 669–683.

Tarantola, A., B., Valette, (1982), Generalised nonlinear inverse problems solved using the least square criterion, *Rev. Geophys.*, *20*, 219-232.

Trampert, J., J.H., Woodhouse, (1995), Global phase velocity maps of Love and Rayleigh waves between 40 and 150 seconds, *Geophys. J. Int.*, *122*, 675–690.

van Heijst, H, and J., Woodhouse, (1997), Measureing surface-wave overtone phase velocities using a mode branch stripping technique, *Geophys. J. Int.*, *131*, 209–230.

van Heijst, H, and J., Woodhouse, (1999), Global high-resolution phase velocity distributions of overtone and fundamental-mode surface waves determined by mode branch stripping, *Geophys. J. Int.*, *137*, 601–620.

Visser, K., S.,Lebedev, J., Trampert, B.L.N., Kennett, (2008), Global Love wave overtone measurements, *Geophys. Res. Lett.*, *34*(L03302), 11–5.

Visser, K., J., Trampert, B.L.N., Kennett, (2008), Global anisotropic phase velocity maps for higher ode Love and Rayleigh waves, *Geophys. J. Int.*, *172*, 1016–1032.

Yoshizawa, K., and B., Kennett, (2002), Determination of the influence zone for surface wave paths, *Geophys. J. Int.*, *149*, 441-454.

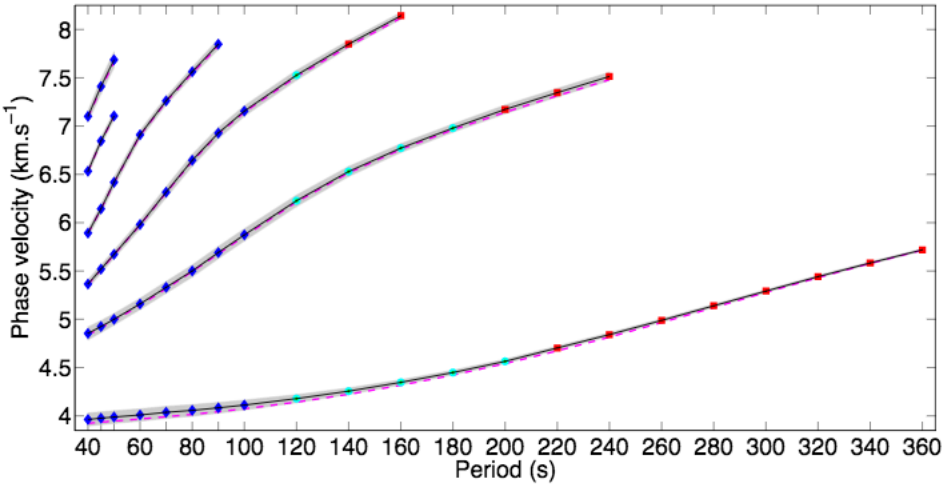

Figure 1. Average dispersion of our entire dataset (black curves) with one standard deviation errors (gray areas). Dispersion curves are shown for the fundamental mode and the first five overtones. Blue diamonds, light blue circles and red squares show periods and modes for which measurements are averaged over *Debayle and Ricard* [2012]'s dataset only, *Debayle and Ricard* [2012]'s dataset plus long period measurements, and only long period measurements, respectively. The dispersion of model PREM (purple dashed curves) is shown for comparison. All phase velocities are corrected from the physical dispersion due to attenuation [*Kanamori and Anderson*, 1977] using a reference period of T= 100 s.

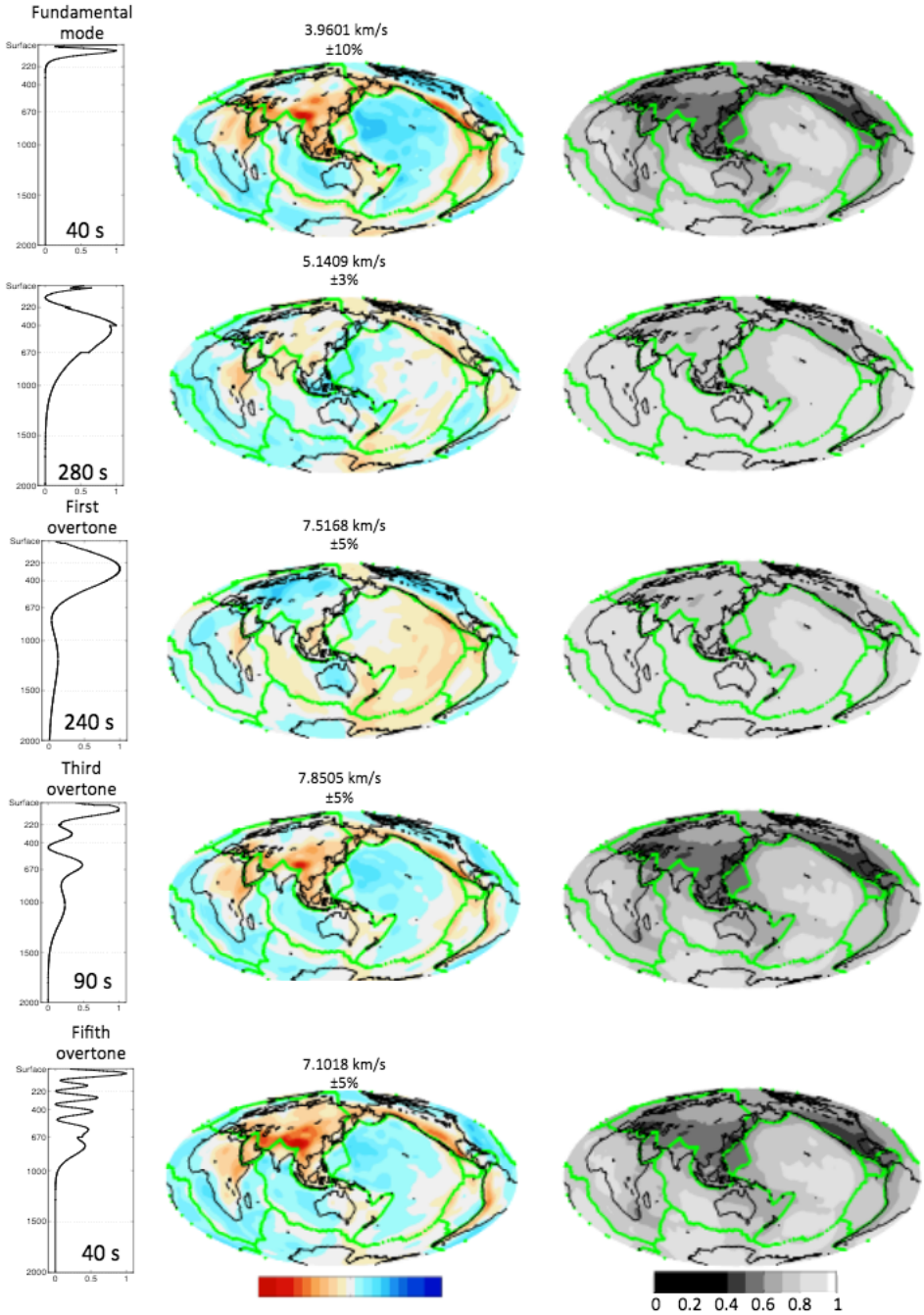

Figure 2. Examples of phase velocity maps (middle column) for some fundamental and higher Rayleigh modes with the corresponding error maps (right column) and V_S sensitivity kernels (left column). Velocity color scales are in percent of a reference value indicated on the top of each map. For the error map shadings, 1 corresponds to an error of 0.05 km s^{-1}.

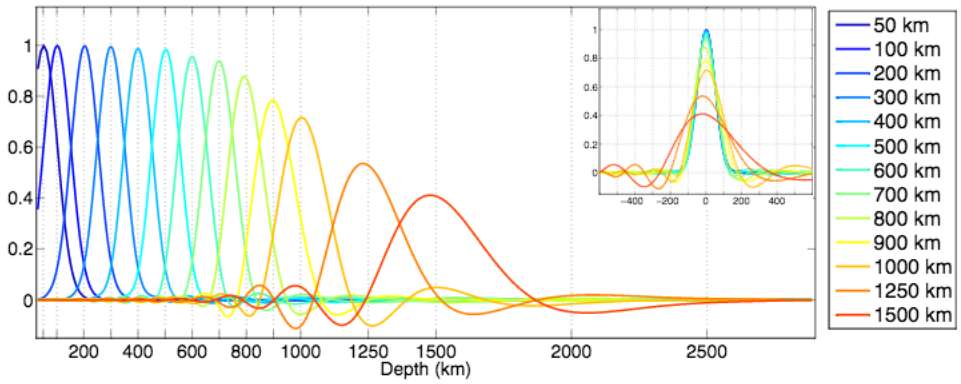

Figure 3. Averaging kernels according to *Backus and Gilbert* [1968]. Same averaging kernels aligned with respect to their maxima (Upper right corner).

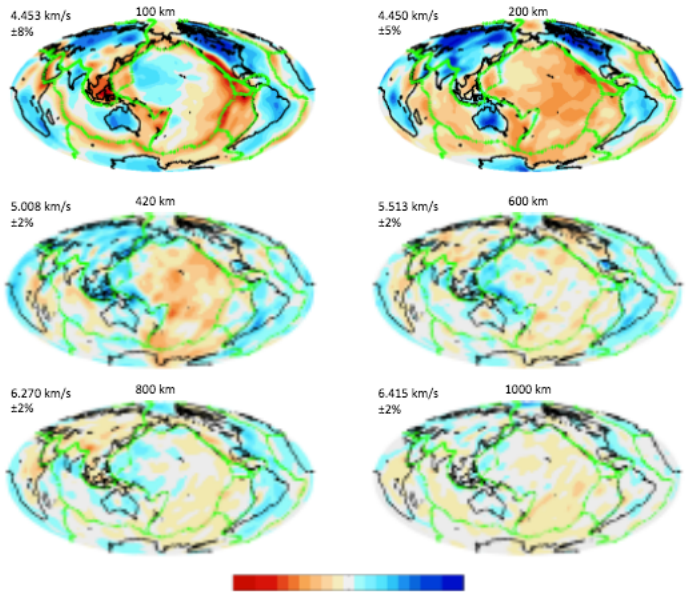

Figure 4. 3D shear velocity model obtained from the inversion of our phase velocity maps. Color scales are in percent of a reference value indicated on the top left corner of each map.

Table 1. Summary of the whole dataset indicating the number of phase velocities measured on the raw dataset and selected to built the phase velocity maps

Mode	Period range (s)	Number of measured periods	Number of raw measurements	Number of selected measurements
Fond. mode	40-360	21	7,270,127	1,559,939
1^{st} overtone	40-240	15	6,088,848	1,159,831
2^{nd} overtone	40-160	11	3,838,851	810,597
3^{rd} overtone	40-90	7	2,608,403	549,864
4^{th} overtone	40-50	3	1,117,887	214,329
5^{th} overtone	40-50	3	1,117,887	238,369
Total		60	22,042,003	4,532,929